 ISSN:1005-748X

SYNTHESIS, STRUCTURAL AND MORPHOLOGICAL ANALYSIS OF NOVEL NICKEL OXIDE NANOHEXAGONS BY HYDROTHERMAL METHOD

S. Virgin Jeba[a], S. Sonia[b] S, N. Annlin Bezy[b] and A. Lesly Fathima[b*]

[a]Research Scholar, Register No. 18113042132018, Research Department of Physics, Holy Cross College (Autonomous), Nagercoil-629004, Tamil Nadu, India.(Affiliated to ManonmaniamSundaranar University, Abishekapatti, Tirunelveli-627012, Tamil Nadu, India)

[b]Research Department of Physics, Holy Cross College (Autonomous), Nagercoil-629004, Tamil Nadu, India.
(Affiliated to ManonmaniamSundaranar University, Abishekapatti, Tirunelveli-627012, Tamil Nadu, India)

[b]*Research supervisor, Research Department of Physics, Holy Cross College (Autonomous), Nagercoil-629004, Tamil Nadu, India.
(Affiliated to ManonmaniamSundaranar University, Abishekapatti, Tirunelveli-627012, Tamil Nadu, India)

Corresponding Author: leslysat@gmail.com

Abstract

Development of different morphologies for materials becomes a phenomenal challenge as they act as the key role in defining their functional properties and desired applications. Here, we report the synthesis of Nickel Oxide (NiO) nanohexagons constructed from their respective nanoscale building blocks through a simple and cost effective hydrothermal technique. Structural analysis based on X-ray diffraction (XRD) confirms the purity of the NiO structures. Field Emission Scanning Electron Microscope (FESEM) corroborates the multiform morphologies of NiO.

Keywords: Nickel Oxide, hydrothermal technique, nanostructures, nanohexagons

1. Introduction

In recent years, synthesis of nanoparticles with various sizes and shapes has received great interest due to their use in emerging technologies. Incredible properties of nanomaterials strongly depend on size and shape of nanoparticles, their interaction with stabilizers and surrounding media and also on their preparation method. To reach better applied characteristics, controlled synthesis of nanocrystals is required [1]. The properties of metal nanoparticles, their size, morphology and stability were influenced by the reaction conditions, interaction of metal ions with reducing agents, and adsorption processes of stabilizing agent with metal nanoparticles [2]. So, by changing the synthesis methods and stabilizing factors, specific control of the shape, size and distribution can be achieved for the nanoparticles produced [3, 4]. Surfactants play an important role in preparing nanomaterials with controlled size and even distribution. In addition they also act as precursors with special structures and shapes which prevent agglomeration. The fact of using surfactant is similar to the reverse - micellar method which is a resourceful route established to produce a variety of nanoparticles [5-8].

On the basis of the unique electrical, optical and magnetic properties Nickel oxide (NiO) has been the subject of a considerable number of research studies [9]. NiO is considered a p-type, wide band gap (3.6–4.0 eV) semiconductor [10, 11]. In accomplishing manipulation of the

nanostructured nickel oxide, a variety of strategies have been employed, such as evaporation [12], sputtering [13], electrodeposition[14], hydrothermal [15]and sol–gel techniques [16]. Hydrothermal method has some advantages such as simple process, low-cost and easiness to obtain high purity products hence it is quite promising and facile route for industrial applications.

The purpose of this work is to synthesis NiO nanohexagons by the hydrothermal process in the presence of HMTA as surfactant, which is a simple way and low in cost since the starting materials are few and inexpensive. The structural analysis, morphological analysis and growth mechanism of the NiO nanostructure was also dealt in detail. Also, the electrochemical performance of the optimized NiO nanohexagons was determined.

2. Experimental

2.1 Materials

Nickel Nitrate hexahydrate $Ni(NO_3)_2.6H_2O$, Ethylene glycol (CH_6O_2), ethanol (C_2H_2OH), aqueous ammonia and Hexamethylenetetramine (HMTA) were of analytical grade and used as received.

2.2 Synthesis of NiO nanohexagons

The hexagons were attained by preparing the NiO nanoparticles using the following process. The 0.3 M $Ni(NO_3)_2$ solution was prepared in DW and EG in the ratio 1:1. Also, 0.1 M urea solution was prepared in the same ratio of DW & EG and added dropwise into the nitrate solution. The pH of nickel nitrate solution was adjusted to 12 by adding aqueous ammonia and continuously stirred for 30 min. Then, 1g of Hexamethylenetetramine (HMTA) was added to the resultant solution and stirred for 2h to make a homogeneous mixture. This homogeneous mixture was further transferred to Teflon lined stainless steel autoclave. The hydrothermal reaction was carried out at 180^{o}C for 12 h and cooled down to room temperature naturally. The final precipitate was washed several times with distilled water to remove the impurities and dried in hot air oven at 100^{o}C. The reactions were carried out in different reaction temperatures: (i) 120^{o}C (ii) 150^{o}C (iii) 180^{o}C. The perfect hexagons were optimized at the reaction temperature of 180^{o}C.

The synthesized NiO samples were authenticated by using F E I Quanta FRG 200- High Resolution Scanning Electron Microscope. Structural analysis of the nanoflowers was performed by X-ray diffraction (XRD) using PANalytical XPert Pro X-ray diffractometer with monochromatic high intensity Cu-K_α radiation (λ = 1.5406 Å). Raman spectra at room temperature were obtained using LABRAM HE Evolution Micro-Raman Spectrometer. The UV-vis spectra of the samples were examined using SYSTRONICS double beam UV-VIS spectrophotometer: 2202 in the wavelength range of 200-800 nm.

3. Results and Discussion

3.1 Structural evolution of NiO nanohexagons

Fig. 1 displays the X-ray diffraction graph of the Nickel Oxide structures grown at different reaction temperatures (120^{o}C, 150^{o}C& 180^{o}C). The crystalline nature was found from the diffraction peaks corresponding to NiO which are strongly visible and perfect. The obtained XRD peaks for all the samples concurs with JCPDS card # 89-5881 thereby confirming the face centered cubic structure. The peaks observed were indexed with the 2θ values corresponding to the crystallographic planes of (222), (400), (440), (622) and (444) respectively. The XRD results show good crystalline structure with high crystallinity. The absence of impurity peaks (such as

 ISSN:1005-748X

$Ni(OH)_2$, Ni_2O_2) shows that the NiO hexagons are of high purity.

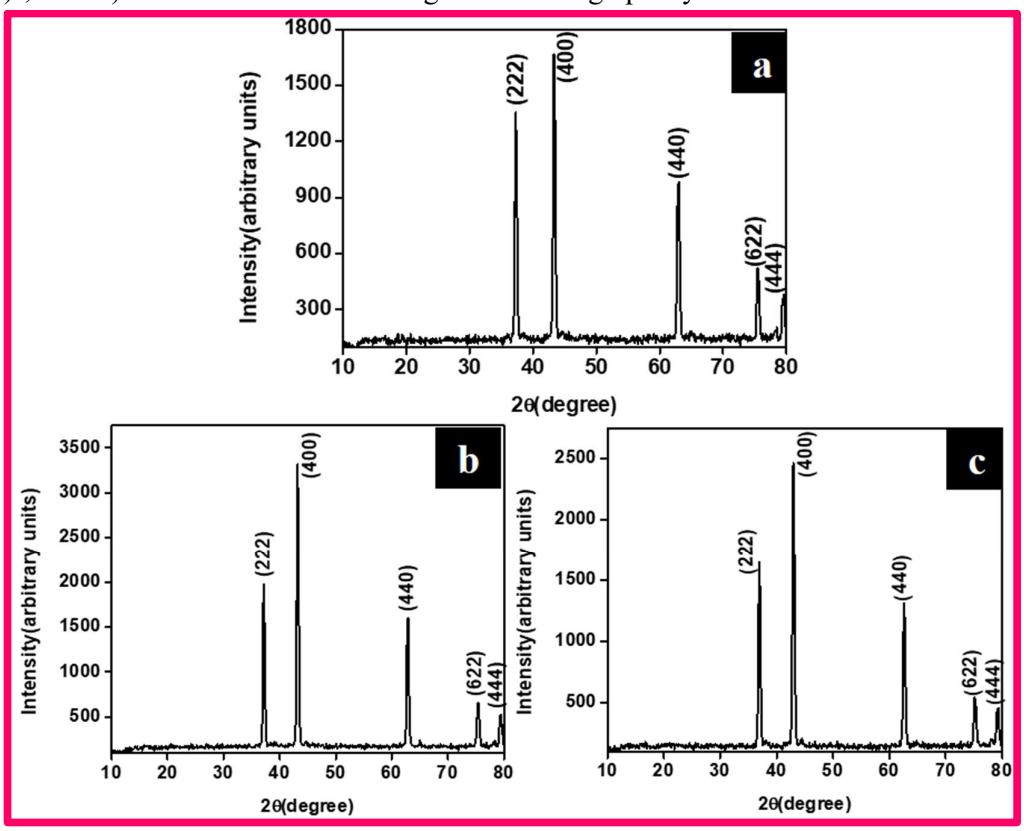

Fig.1. XRD pattern for NiO nanohexagons with different reaction temperatures

(a) 120°C (b) 150°C (c) 180°C

3.2.1 Estimation of crystallite size and lattice strain

Average crystallite size was determined from broadening of X-ray diffraction peaks by the well-known Scherrer equation is expressed as [17]

$$\beta_D = \frac{k\lambda}{\beta \cos\theta}$$

Where β_D is the FWHM (ie, broadening of the peak) in radians, k=0.9 is the geometry factor, λ=1.5406 Å is the wavelength of X-ray source, D is the crystallite size and θ is the peak position in radians. The average crystallite sizes of the samples prepared with 120°C, 150°C and 180°C of reaction temperature is 24 nm, 23 nm and 22 nm respectively. Also, the lattice parameter estimated from XRD patterns of the samples is 8.3487 Å, 8.365 Å and 8.398 Å respectively for the samples synthesized with reaction temperatures 120°C, 150°C and 180°C.

The W-H plot is used to determine the crystallite size and lattice strain from the broadening of the X-ray diffraction peaks by considering the FWHM of all the individual peaks. The Williamson and Hall plots for NiO nanostructures synthesized in 120°C, 150°C and 180°C are shown in **Fig 2**. A linear fit of the scattered results is taken into consideration. From this linear fit, the crystallite size and strain were estimated from the y-intercept and slope of the fit respectively. Lattice strain is a measure of lattice dislocations, which arise due to crystal imperfections [18].

From W-H plotting it is proved that the average particle size D is 29 nm, 27 nm and 25 nm, for the samples grown in 120°C, 150°C and 180°C reaction temperature respectively, which is in good agreement with the values determined by Scherer's formula. The microstrain of the

 ISSN:1005-748X

optimized NiO hexagons is about 0.0002863, where the positive value of the lattice strain (ε>0) shows that the strain in the crystal is tensile [19].

At 120°C growth, the crystallite size for hexagons is 29 nm, which is reduced to 25 nm in comparison with crystalline size grown at 180°C reaction temperature. The reason for reduction of crystalline size may be due to the increase in growth temperature as it controls the aggregation of the material and favours the reduction reaction. The thermodynamics of the reaction changes due to the disparity in the temperature thereby favouring the differential growth [20].

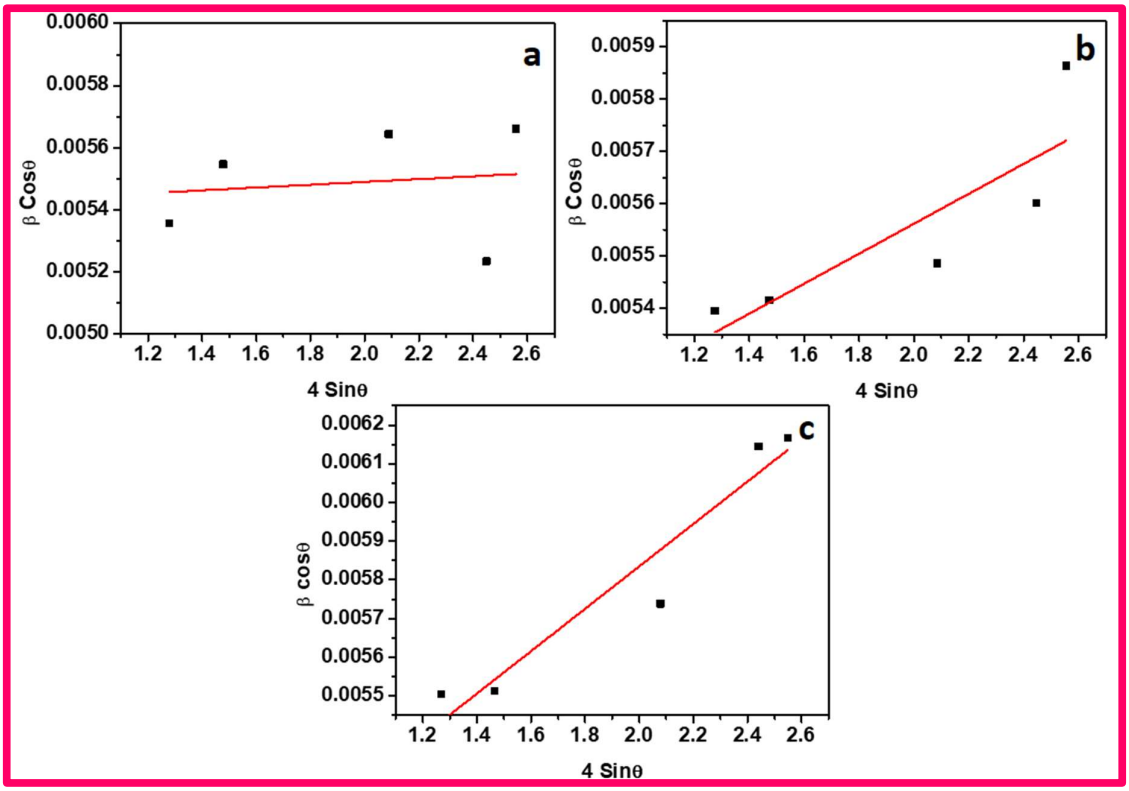

Fig.2. Williamson and Hall plot for NiO nanohexagons with different reaction temperatures

(a) 120°C (b) 150°C (c) 180°C

3.3 Morphological analysis of hexagons

The FESEM images depict morphological features of NiO nanostructures in **Fig 3**. The perfect hexagon shape was optimized by adjusting the reaction temperature from 120°C to 180°C. From **Fig (3a)**, it is seen that the nucleation results in incomplete growth due to average-proficient when the reaction temperature is 120°C, which leads to incomplete formation of the hexagons. The initial formation of hexagons is visible in the FESEM image. The NiO hexagons formation at reaction temperature 150°C (**Fig 3b**) were not well oriented and dispersed As the reaction temperature increased to 180°C, the particles turned to perfect hexogons and uniform growth is observed which is shown in **Fig 3c**.

The nucleation rate increases more swiftly due to supersaturation, which was optimized by the pH of the reaction and increase in temperature. At this higher temperature, formation of crystal nucleus was prompted, which causes nuclear aggregation. The rate of aggregation controls the morphology and structure of the resulting product [21].

As the decomposition rate of HMTA is very high, in higher temperature the rate of OH^- supply increases. The gaseous products were eliminated faster from the reaction which gives rise

 ISSN:1005-748X

to capillary forces on the seed which leads to the interaction of particles with each other. This causes more particle agglomeration, cluster formation and particle growth [22]. Therefore, there is a drastic increase in their growth rate. This increased growth rate leads to the formation of hexagon shaped structure with sharp edges.

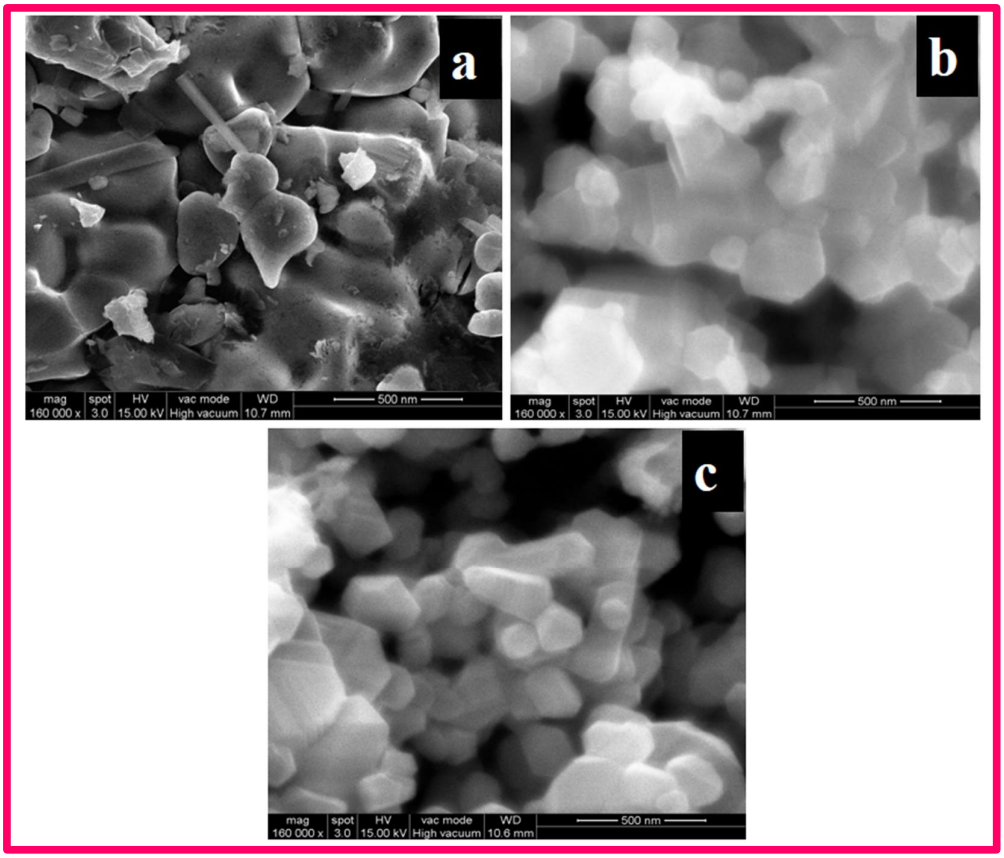

Fig.3. FESEM image ofNiOnanohexagons with different reaction temperatures

(a) 120ºC (b) 150ºC (c) 180ºC

The magnified image of NiO nanohexagons is clearly shown in **Fig 4a**. The EDS results of all the chemically derived NiO nanostructures showed the presence of Ni and O elements as shown in **Fig 4b**. The chemical compositions have been listed in the table (insets). In addition, there was no evidence of impurities or residues observed in the EDS results, which also confirmed the purity and complete formation of NiO nanostructures.

 ISSN:1005-748X

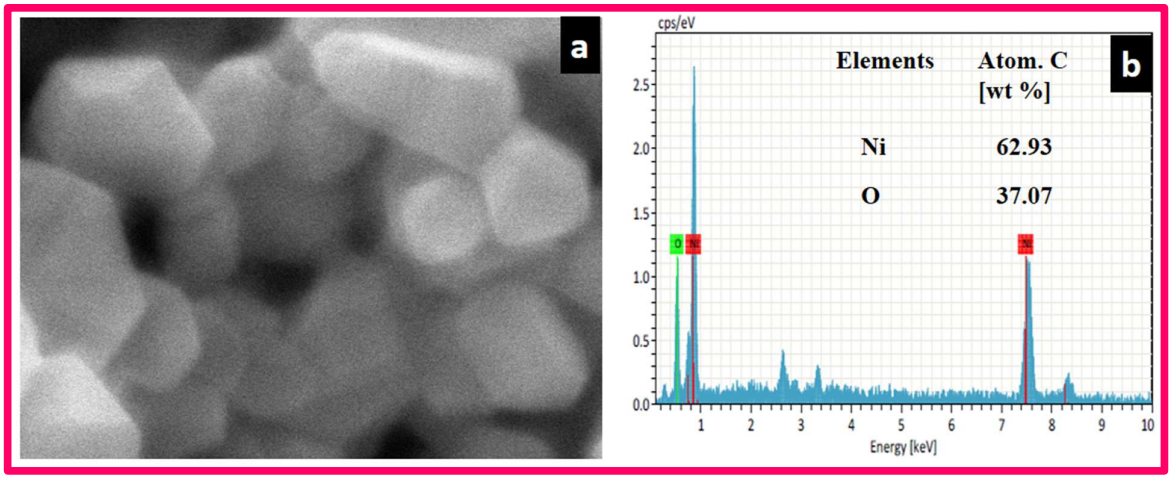

Fig.4. (a) Magnified image of NiO nanohexagons (b) EDS spectra of the optimized nanohexagons

3.4 Raman analysis of NiO nanohexagons

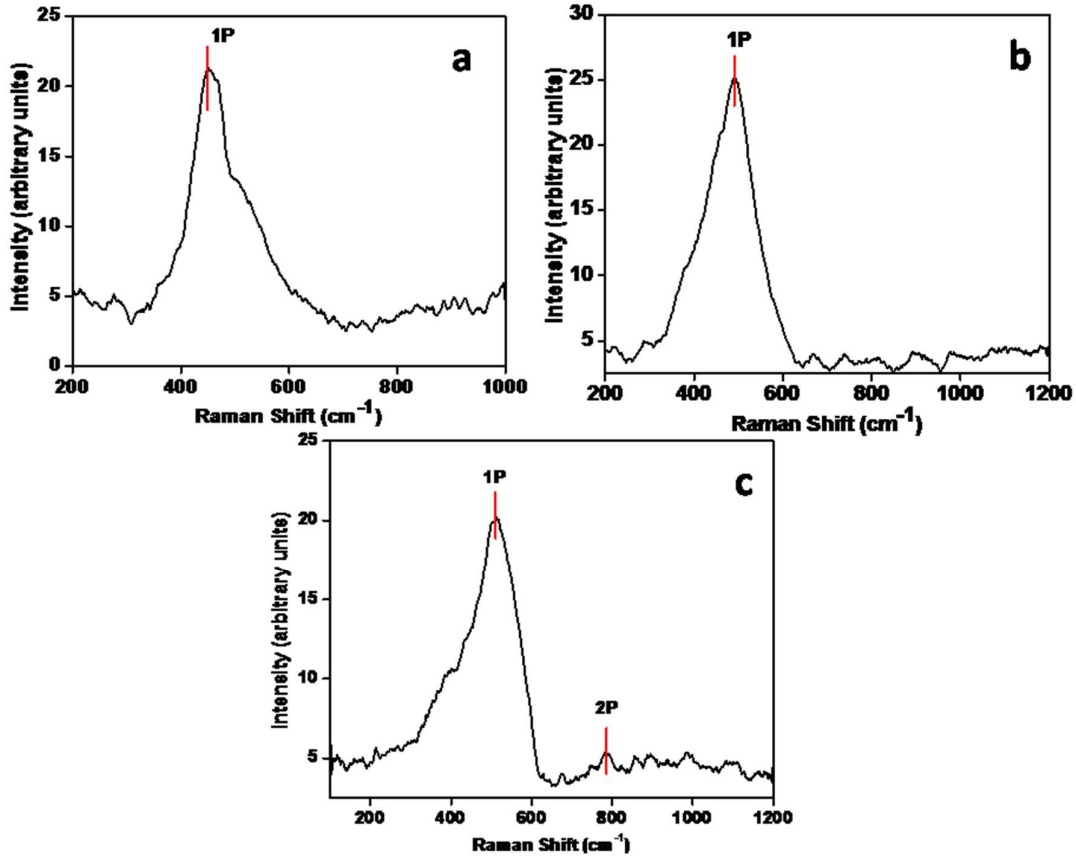

Fig. 5 Raman spectra of NiO nanohexagons with different reaction temperatures (a) 120°C (b) 150°C (c) 180°C

The Raman spectra of NiO nanohexagons were obtained with the assistance of a Raman spectrometer by employing an argon laser with a wavelength of 488 nm and a continuous-wave power of 5 mW as the excitation source. Using a LABRAM HE Evolution Micro-Raman spectrometer, Raman spectra of NiO nanohexagons were acquired in a backscattering mode at

 ISSN:1005-748X

room temperature. To analyze the NiO nanohexagons, an argon-ion laser with a wavelength of 514.14 nm is employed as the excitation source. The results can be seen in **Fig. 5**. The Ni-O stretching mode of vibration was responsible for the strong and broad peak that appeared in the Raman spectra at 518 cm^{-1} (1LO mode). The transition of NiO nanoparticles from an antiferromagnetic state to a superparamagnetic state is shown by the absence of a magnon peak in the Raman spectra between 1000- 1500 cm^{-1}. We compare the high-intensity peak at 500 cm^{-1} to the expected phonon and magnon modes for a single cubic NiO crystal and based on this comparison, we determine that the peak is due to LO phonon modes. With the help of this comparison, we were able to identify the modes that had contributed to the peak. It should come as no surprise that the sample does not have a magnon peak. In **Fig. 5 (c)**, the increases were brought about by the sintering temperature. The relative intensity of the LO phonon mode increases as the size of the sample decreases, which is suggestive of a rise in the number of nickel vacancies. This confirms that the annealing caused a change in the composition of the NiO powder to a non-stoichiometric form with an excess of oxygen atoms and identifies a portion of the NiO NPs as having a composition that is close to Ni_2O_3. It also characterizes that portion of the thin film as having a composition that is close to Ni_2O_3. As a direct consequence of this, an excessive amount of oxygen in NiO produces openings in the typically filled Ni sites. Therefore, a p-type semiconductor can be formed from NiO with an excess of oxygen [23].

3.5 UV-vis analysis of NiO nanohexagon

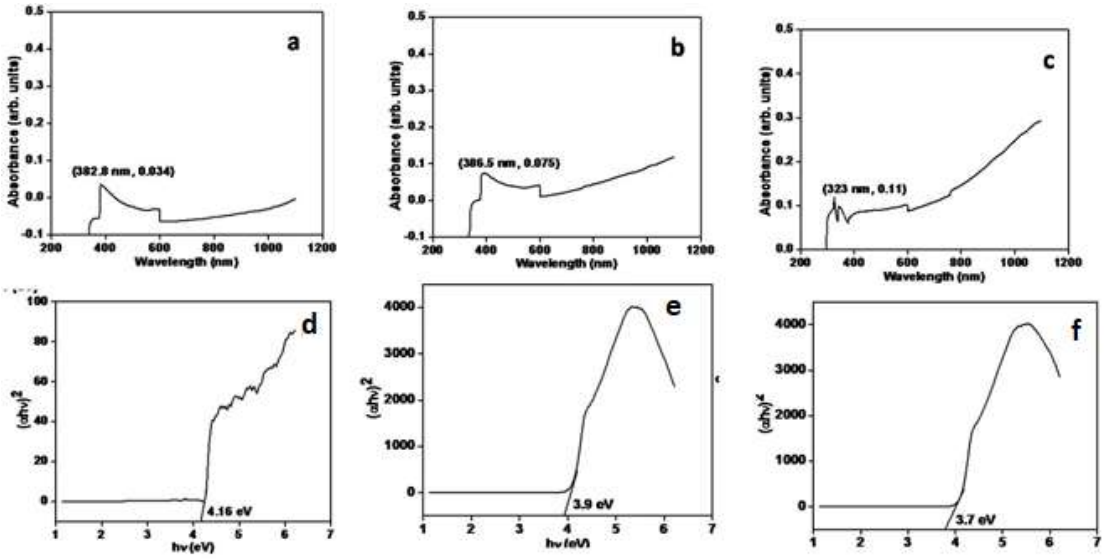

Fig. 6 (a-c) UV Visible absorption spectrum of dumbbell shaped NiO using various temperature (120 °C,150 °C and 180 °C) and (d-f) Tauc's plot of dumbbell shaped NiO using various amount of NaOH concentration (120 °C, 150 °C and 180 °C)

Fig. 6 (a-c) shows NiO NPs UV-Visible spectra and bandgap at temperatures 120 °C, 150 °C, and 180 °C between wavelength 200 to 800 nm. The spectra showed the presence of absorption peaks at 382.8, 386.5, and 323 nm that are caused by the electronic transition from VB to CB of the Nickel 3-d orbital and the 2-p orbital of Oxygen. The following equation [24] can be used to determine the energy bandgap of NiO-NPs at various sintering temperatures.

$$(\alpha h\upsilon)1/n = A(h\upsilon - Eg)$$

where

 ISSN:1005-748X

Eg = bandgap energy,
hv (eV) = photon energy,
a = absorption coefficient,
A represents a constant n = 2 in direct transition,

NiO NPs calculated bandgap was determined and is shown in **Table 1**. The energy band values were found to be relatively near to the NiO bandgap energies previously reported in the literature, which range from 3.4 to 3.8 eV [25]. Crystallite growth reveals that the bandgap shrinks as the temperature of the calcination increases. The competition between the nucleation and growth processes has led to an increase in crystal size and, as a result, a decrease in the bandgap at higher temperatures. According to our research, a boost in reaction temperature caused Ni^{+} ions to rapidly deplete, which then gave birth to NiO nanoparticles with reduced crystallite sizes. The synthesis of NiO nanoparticles at lower temperatures (120 °C), although nucleation was more beneficial at higher temperatures (180 °C), may result in the formation of smaller crystallite sizes [26].

Table 1. Optical parameters of NiO nanohexagons

Wavelength (nm)	Absorbance	Bandgap	Temperature (°C)
382.8	0.034	4.16	120
386.5	0.075	3.9	150
323	0.11	3.7	180

3.6 Photoluminescence (PL) analysis of NiO nanohexagons

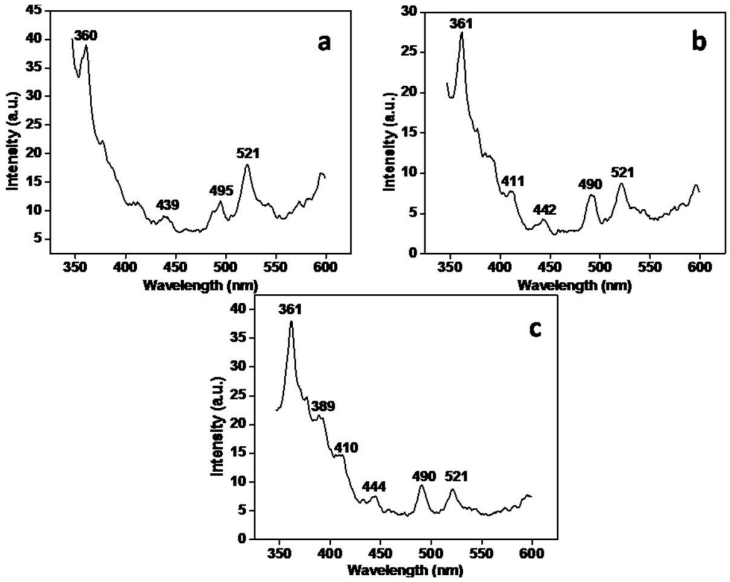

Fig. 7 Photoluminescence spectra of NiO nanohexagons with different reaction temperatures (a) 120ºC (b) 150ºC (c) 180ºC

Fig. 7 displays the 350–600 nm photoluminescence (PL) emission spectra of hexagonal-shaped NiO NPs sintered at 120, 150, and 180 °C. For instance, **Fig. 7 (a-c)** exhibits a wide UV emission band in the range of ~ 360 nm and a shoulder peak in the visible spectrum centred in the range of ~ 439, 495 and 521 nm [27]. Sample (c) displays a red shift and a narrowing peak compared to the other two. In contrast to the other two samples, sample (c) did not exhibit a significant increase in emission intensity by the phenomenon of exciton-exciton scattering. The

 ISSN:1005-748X

intrinsic transitions of the exciton from the conduction band of Ni to the valance band valence band of Ni, electronic transition involving the $3d^8$ electrons of the Ni^{2+} ions [28]. Surface oxygen vacancies are represented at 435–445 and 490–495 nm which confirmed the blue emission of all samples (a-c). The band at in the region of 521 nm, is due to the occurrence of green emission this is due to the increase in defect levels in the crystals caused by these oxygen vacancies [29]. Due to cation vacancies, interstitial oxygen trapping in surface of NiO NPs induces the green band emission observed at 521 nm by the action by charge transfer mechanism between Ni^{2+} and Ni^{3+} ions [30-31]. As a consequence of the inhibition of the electron-hole recombination process, tiny particles with large Ni vacancies when excited will result in a decrease in PL intensity spectrum when the calcination temperature gets higher. Low PL intensity is associated with extended photogenerated carrier lifetimes and low recombination centre density.

3.7 Electrochemical performance of NiO nanohexagons

Fig. 8 (a-c) display the electrochemical performance of NiO nanohexagons. **Fig. 8** displays the CV curve of NiO NPs at different scan rates (1-50 mVs^{-1} at a potential window of 0-0.5 V). Platinum wire is utilized as the counter electrode and the SCE electrode is used as the reference electrode in a three-electrode configuration. The entire CV curve shows two separate redox peaks that are associated with the reversible conversion of Ni^{2+} into Ni^{3+}. The CV curves essentially maintain the same profiles with a slight shift in the peak location, showing fast diffusion of the involved ions and excellent reversibility of the redox reaction at the electrode electrolyte interface. As can be seen, the kinetic responsiveness of electrochemical current improves with increasing scan rate. Galvanostatic charge/discharge profiles produced at various current densities also display a non-linear connection in a manner similar to this, as shown in the in figure (b). Each CD curve has a peak that denotes a redox transition, which is compatible with the voltametric graph. The projected specific capacitance values for the synthesized NiO NPs at 120, 73, 67, 60, 55, and 50 $F.g^{-1}$ at 0.9, 1.8, 2.7, 3.6, 4.5, and 7.2 $A.g^{-1}$ are shown in **Fig. 8 (c)**. It is well known that the region surrounding the CV curves and the specific capacitance are related. Additionally, it unambiguously demonstrates how, at high current densities, the specific capacitance drops off due to insufficient electrode ion diffusion at the electrode surface during fast charge and discharge mechanisms.

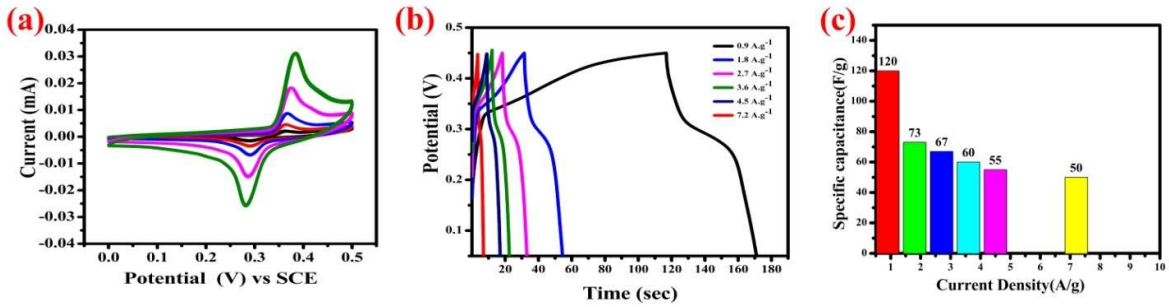

Fig. 8 (a) CV (cyclic voltammetry) curves at 1-50 mVs^{-1} scan rate; (b) G-CD (galvanostatic charge-discharge) curves at 0.9-7.2 A g^{-1} current density; (c) specific capacitance of the NiO NPs electrodes at different current densities.

3. Conclusion

NiO nanohexagons was successfully synthesized by facile hydrothermal process under mild reaction medium, by varying the temperature. Structural analysis reveals the phase purity and

crystallinity of the designed NiO nanohexagons. The distinct and well-aligned nanohexagons of NiO was confirmed by the morphological analysis. Furthermore, the electrochemical performance of the synthesized NiO nanohexagons was examined.

References

[1] Amany ,A., El-Rab, S.F.G., 2012. Effect of reducing and protecting agents on size of Silver nanoparticles and their anti-bacterial activity. Der Pharma Chemica. 4 (1),53-65.

[2] Ghorbani, H. R., Safekordi , A.A., Attar, H., Rezayat Sorkhabadi, S. M., 2011. Biological and Non-biological Methods for Silver Nanoparticles Synthesis, Chem Biochem Eng Q. 25 (3),317-326.

[3] Yeo, S., Lee, H .,Jeong,S., 2003. Antibacterial effect of nanosized silver colloidal solution on textile fabrics. J. Mater. Sci. 38, 2143-2147.

[4] Zhang, J., Chen, P., Sun, C., Hu ,X., 2004. Sonochemical Synthesis of Colloidal Silver Catalysts for Reduction of Complexing Silver in DTR System. Appl. Catal. A. 266,49-54

[5] Zhang D, Qi L, Ma J, Cheng H, J Mater Chem. 12 (2002) 3677.

[6] Pileni M P. Reverse micelles: A microreactors. J. Phys Chem. 97 (1993) 6961.

[7] Ahmad T, Ganguli A K, J. Am Ceram Soc. 89 (2006) 1326.

[8] Ahmad T, Kavitha G, Narayana C, Ganguli A K, J. Mater Res. 20 (2005) 1415.

[9] E.R. Beach, K.R. Shqau, S.E. Brown, S.J. Rozeveld, P.A. Morris, Mater. Chem. Phys. 115 (2009) 371– 377.

[10] H.-L. Chen, Y.-M. Lu, W.-S. Hwang, Surf. Coat. Technol. 198 (2005) 138–142.

[11] H. Sato, T. Minami, S. Takata, T. Yamada, Thin Solid Films 236 (1993) 27–31.

[12] R. Cinnsealach, G. Boschloo, S.N. Rao, D. Fitzmaurice, Solar Energy Mater. Solar Cells 57 (1999) 107–125.

[13] K. Yoshimura, T. Miki, S. Tanemura, Jpn. J. Appl. Phys. 34 (1995) 2440–2446.

[14] C. Natarajan, H. Matsumoto, G. Nogami, J. Electrochem. Soc. 144 (1997) 121–126.

[15] MasoudSalavati-Niasari, HamidehSeyghalkar, OmidAmiri, FatemehDavar, J. Clust Sci24 (2013) 365–376

[16] A. Surca, B. Orel, B. Pihlar, P. Bukovec, J. Electroanal. Chem. 408 (1996) 83–100.

[17] Cullity B D 1956, Elements of X-ray Diffraction. Addison-Wesley Publishing Company Inc. California.

[18] Zak A K, Abd. Majid W H, Abrishami M E and Yousefi R 2011 Solid State Sciences 13 251– 256.

[19] B. Yahmadi a, N. Kamouna, C. Guaschb, R. Bennaceur a, Materials Chemistry and Physics 127 (2011) 239-247.

[20] A. Thankappan, M. Hari, S. Mathew, S.A. Joseph, E. Rolf, D. Bora, A. Braun, V.P.N. Nampoori, Phys. E: Low-Dimens. Syst. Nanostruct. 44 (2012) 2118–2123.

[21] M.R. Parra, F.Z. Haque, J.Mater. Res. Technol. 3 (2014) 363–369.

[22] M. Farhadi-Khouzani, Z. Fereshteh, M.R. Loghman-Estarki, R.S. Razavi, J. Sol-Gel Sci. Technol. 64 (2012) 193–199.

[23] Deshpande, M., et al. Structural, thermal and optical properties of nickel oxide (NiO) nanoparticles synthesized by chemical precipitation method. in Advanced Materials Research. 2016. Trans Tech Publ.

[24] Murphy, A., Band-gap determination from diffuse reflectance measurements of semiconductor films, and application to photoelectrochemical water-splitting. Solar Energy Materials and Solar Cells, 2007. 91(14): p. 1326-1337.
[25] Sasi, B. and K. Gopchandran, Nanostructured mesoporous nickel oxide thin films. Nanotechnology, 2007. 18(11): p. 115613.
[26] Mahmoodian, H., et al., Enhanced removal of methyl orange from aqueous solutions by poly HEMA–chitosan-MWCNT nano-composite. Journal of Molecular Liquids, 2015. 202: p. 189-198.
[27] Faisal, M., et al., Novel mesoporous NiO/TiO2 nanocomposites with enhanced photocatalytic activity under visible light illumination. Ceramics International, 2018. 44(6): p. 7047-7056.
[28] Wu, Z., et al., An ultrasound-assisted deposition of NiO nanoparticles on TiO 2 nanotube arrays for enhanced photocatalytic activity. Journal of Materials Chemistry A, 2014. 2(22): p. 8223-8229.
[29] Abdur Rahman, M. and R. Radhakrishnan, Microstructural properties and antibacterial activity of Ce doped NiO through chemical method SN Appl. 2019, Sci.
[30] Chauhan, J. and U. Chaubey, Synthesis and characterization of neodymium doped nickel oxide nanoparticles. Synthesis, 2018. 8(4).
[31] Gandhi, A.C. and S.Y. Wu, Strong deep-level-emission photoluminescence in NiO nanoparticles. Nanomaterials, 2017. 7(8): p. 231.